Automatic crack tip detection and stress intensity factors estimation of curved cracks from digital images

Julien Réthoré

INTERNATIONAL JOURNAL FOR NUMERICAL METHODS IN ENGINEERING

Int. J. Numer. Meth. Engng 2013; **00**:1–**??**

Published online in Wiley InterScience (www.interscience.wiley.com). DOI: 10.1002/nme

Automatic crack tip detection and stress intensity factors estimation of curved cracks from digital images

J. Réthoré*

LaMCoS, Université de Lyon / INSA Lyon / CNRS UMR 5259

27 Avenue Jean Capelle, F-69621 Villeurbanne, France.

SUMMARY

With the development of full-field measurement techniques, it has been possible to analyze crack propagation experimentally with an increasing level of robustness. However, the analysis of curved cracks is made difficult and almost unexplored because the possible analysis domain size decreases with crack curvature, leading to an increasing uncertainty level. This paper proposes a digital image correlation technique, augmented by an elastic regularization, combining finite element kinematics on an adapted mesh and a truncated Williams' expansion. Through the analysis of two examples, the proposed technique is shown to be able to address the experimental problems of crack tip detection and stress intensity factors estimation along a curved crack path.

Received ...

KEY WORDS: curved crack; stress intensity factors; crack tip detection; finite element; Williams' series; digital image correlation

*Correspondence to: LaMCoS, Université de Lyon / INSA Lyon / CNRS UMR 5259

27 Avenue Jean Capelle, F-69621 Villeurbanne, France.

1. INTRODUCTION

With the development of full-field measurement techniques, it has been possible to analyze experimentally crack propagation with an increasing level of robustness. The improvement of the robustness is directly related to the increasing amount of data available for the analysis. For crack tip fields analysis, this robustness basically depends on the size of the domain used for experimental stress intensity factors extraction. The analysis of curved cracks is made difficult and almost unexplored because the possible extraction domain size, and thus the maximum robustness, decreases as the crack curvature is increasing. The experimental estimation of the crack tip position is also a difficult question in this context.

The most common practice to estimate stress intensity factors (SIF) at the tip of a crack relies on a post-processing of the displacement or strain/stress fields. Analyzing the displacement field leads to a least-squares projection onto an appropriate basis. This technique has been used either in numerical simulations *e.g.* [1] or in the post-processing of experimental 2D or 3D full displacement field measurements *e.g.* [2, 3, 4, 5, 6, 7]. Extracting SIF from strain/stress fields is usually based on Linear Elastic Fracture Mechanics theory and path independent integrals. This kind of technique is extremely popular for numerical simulations and it has been used in a number of different cases in 2D or in 3D: quasi-static crack propagation, cohesive fracture, confined plasticity, fretting with contact and friction between the crack faces, dynamic crack propagation. The interaction integral has also been used to extract SIF in 2D [8] and in 3D [9] from experimental displacement fields measured by digital image or volume correlation. However, due to the derivation of the displacement field to obtain the strain field, the noise sensitivity of this class of strain/stress based techniques is higher than for displacement based methods. Even if the noise sensitivity of the interaction integral can be optimized [10], it has been shown in [11] that displacement based techniques have lower noise sensitivity. The conclusion of this paper is that the best accuracy

Prepared using nmeauth.cls DOI: 10.1002/nme

is obtained when SIF are directly estimated, *i.e.* when they are among the degrees of freedom of the problem to solve as in [5]. This remark applies not only for experimental displacement fields but also for numerical simulations for which different strategies have been proposed for direct estimation of SIF. These strategies have been developed in the context of the eXtended Finite Element Method (X-FEM) [12, 13] and they recover optimal convergence in terms of SIF if the underlying partition of unity finite element functions are inactivated over the SIF extraction zone [14, 15, 16]. The latter two references make use of the coupling between an X-FEM model and an analytical basis based on a truncation of the Williams' series [17]. The coupling of the two models is achieved either by a partition of the energy over an overlapping domain [15] or with a Mortar method [16]. These two methods were shown to be able to simulate the propagation of a crack under loading conditions leading to a curved crack path [18, 19].

The use of the Williams' series (obtained for a straight crack) to track curved cracks requires that the size of the extraction domain over which they are used as displacement basis functions is small compared to the local crack curvature. For numerical simulations, the performance of the direct SIF extraction is related to the ratio between the extraction domain size and the mesh size in the vicinity of the crack tip. The mesh is thus refined to obtain an objective performance level given the extraction domain size appropriate to the crack curvature. From the experimental point of view, the existing technique for direct SIF estimation from digital images was proposed in [5]. In the latter, the optical flow equation is solved over a circular domain centered at the presupposed crack tip and Williams' series are used as displacement basis functions. The performance of the SIF extraction in terms of accuracy and noise sensitivity is again linked to the extraction domain size which has to be as large as possible. This constraint is not compatible with the analysis of curved cracks for which the extraction domain has to be compared to the crack curvature. For this reason, the method proposed in [5] is not suitable for the experimental analysis of curved cracks. This is also the case for

Prepared using nmeauth.cls
DOI: 10.1002/nme

the methods cited above that can be used for extracting mixed-mode SIF, but not along curved crack.

Concerning the determination of the crack tip position from experimental displacement fields, the crack tip coordinates can be included in the least-squares minimization process between the experimental displacement field and the analytical basis [4]. However, a more robust approach relies on the concept of an elastic crack tip and its detection using the first super-singular term of the Williams' expansion [20]. This approach reveals robust with respect to a non-linear process zone due to plasticity [21], diffuse damage [22] or cohesive fracture [23]. It has been shown to be robust enough for real time detection of crack propagation for load shedding in fatigue crack propagation experiments [24].

This paper is aimed at proposing a methodology that allows for the analysis of curved cracks using digital images. It includes the detection of the crack path, the detection of the crack tip and the estimation of SIF and higher order terms like the T-stress. The proposed method uses a truncated Williams' expansion as the displacement basis function in the crack tip vicinity. The direct estimation of the Williams' expansion terms is obtained through a condensation of the degrees of freedom of a finite element model using mesh adaptation at the crack tip. The issue of decreasing noise robustness due decreasing extraction domain size, required by the crack curvature, is solved by adding a supplementary elastic regularization term to the optical flow equation. The paper is organized as follows: first the methodology for direct SIF estimation is described, then the formulation of the optical flow equation with elastic regularization is detailed. Then, the implementation of the methodology is described. Last, two examples are analyzed. The first example consists of the analysis of artificially generated images and the second example considers an experiment on a sample geometry and loading conditions leading to a curved crack propagation.

Prepared using nmeauth.cls
DOI: 10.1002/nme

2. DIRECT SIF ESTIMATION

For the direct estimation of SIF, a truncation of the Williams' expansion is used in combination with a finite element model. This section details how these two descriptions are combined to obtain a direct SIF estimation. These descriptions require that two coordinate systems are defined (see Figure 1):

- the global frame (X,Y) associated with the structure
- the local frame at the crack tip (x,y) aligned with the crack

In the following, we adopt a finite element discretization for the displacement field. The discretized displacement field reads:

$$\boldsymbol{u}_{FE}(\mathbf{X}) = \sum_{k=1\ldots 2N} u_k \boldsymbol{N}_k(\mathbf{X}) = [\mathbf{N}]\{\mathbf{U}\}, \tag{1}$$

where N is number of nodes, leading to $2N$ degress of freedom (DOF), and $\boldsymbol{N}_k$ the finite element shape functions. Odd, respectively even, k index corresponds to a DOF along X, respectively Y. A compact notation is adopted in the following: to collect the values of the displacement at the evaluation points, a matrix form of this equation is also used: $[\mathbf{N}]\{\mathbf{U}\}$, where $[\mathbf{N}]$ is a matrix that collects the value of the $2N$ shape functions at the evaluation points and $\{\mathbf{U}\}$ the vector that collects the values of the displacement DOF. Note that $[\mathbf{N}]$ has $2N$ columns and as many lines as points where the shape functions are evaluated. For clarity, the positions of these evaluation points are omitted by the notation.

2.1. Williams' series

For a 2D elastic body with a semi-infinite straight crack subjected to a mechanical load, an analytical solution for the displacement field was proposed by [17]. The displacement is decomposed over a double series of $\boldsymbol{\phi}_j^n$ solution fields that satisfy stress-free conditions along the crack faces. Two fracture modes (indexed by j) are usually distinguished: mode I (opening mode) and mode II (shear mode). These elementary solutions are indexed by

Prepared using nmeauth.cls
DOI: 10.1002/nme

n, and are written as follows:

$$\boldsymbol{\phi}_I^n(r,\theta) = r^{n/2}\left(\kappa e^{in\theta/2} - \frac{n}{2}e^{i(4-n)\theta/2} + (\frac{n}{2}+(-1)^n)e^{-in\theta/2}\right) \tag{2}$$

and

$$\boldsymbol{\phi}_{II}^n(r,\theta) = ir^{n/2}\left(\kappa e^{in\theta/2} + \frac{n}{2}e^{i(4-n)\theta/2} - (\frac{n}{2}-(-1)^n)e^{-in\theta/2}\right). \tag{3}$$

In these equations, i is the pure imaginary number, r the distance to the crack tip and θ the angle with respect to the coordinate system (x,y) aligned with the crack. Hence, adopting complex notations, the position of a material point is defined by z which can be expressed as $x+iy$ or by $r\,e^{i\theta}$. κ is the Kolossov's constant, namely, $\kappa=(3-\nu)/(1+\nu)$ for plane stress or $\kappa=(3-4\nu)$ for plane strain conditions, where ν is the Poisson's ratio.

This family of solutions is the appropriate basis to describe the displacement field around the tip of a crack. It contains:

$n=0$ rigid body translations

$n=1$ usual asymptotic terms that are weighted by stress intensity factors

$n=2$ rigid body in-plane rotation and T-stress

$n>2$ sub-singular terms, *i.e.* the corresponding elastic stress field is not singular at the crack tip.

Usually, only $n\geq 0$ terms are considered because $n<0$ terms exhibit an infinite strain energy density at the crack tip. An actual displacement field $\boldsymbol{u}_w$, determined over the previously introduced basis is:

$$\boldsymbol{u}_w = \sum_{j=I,II}\sum_{n=n_m\ldots n_M} a_j^n \bar{\boldsymbol{\phi}}_j^n(z). \tag{4}$$

In this equation, n_m and n_M define the truncation of the Williams' expansion that is considered and $\bar{\boldsymbol{\phi}}_j^n$ the projection of $\boldsymbol{\phi}_j^n$ onto the X,Y coordinate system.

2.2. Condensation

On the sample surface, the displacement field is described using a finite element model. Within the extraction domain Ω_K surrounding the crack tip, a condensation technique

Prepared using nmeauth.cls DOI: 10.1002/nme

is used in order to reduce the finite element kinematics to the truncated Williams' expansion. The condensation is written as a linear operator between the finite element DOF of the entire mesh $\mathbf{U}$ and the reduced basis $\mathbf{U}_r$:

$$\{\mathbf{U}\} = [\mathbf{L}]\{\mathbf{U}_r\}. \tag{5}$$

For the nodes outside the extraction domain, the condensation operator $\mathbf{L}$ reduces to a diagonal matrix. For the nodes within the extraction domain, the displacement is given by the $\boldsymbol{\phi}_j^n$ functions evaluated at the corresponding node position. The expression of the condensation operator $\mathbf{L}$ is thus given by

$$\mathbf{L} = \begin{pmatrix} 1 & & & & & & & \\ & \ddots & & & & & & \\ & & 1 & & & & & \\ & & & \bar{\boldsymbol{\phi}}_I^{n_m}(r_{i_o},\theta_{i_o}) & \dots & \bar{\boldsymbol{\phi}}_I^{n_M}(r_{i_o},\theta_{i_o}) & \bar{\boldsymbol{\phi}}_{II}^{n_m}(r_{i_o},\theta_{i_o}) & \dots & \bar{\boldsymbol{\phi}}_{II}^{n_M}(r_{i_o},\theta_{i_o}) \\ & & & \vdots & \vdots & \vdots & \vdots & \vdots & \vdots \\ & & & \bar{\boldsymbol{\phi}}_I^{n_m}(r_N,\theta_N) & \dots & \bar{\boldsymbol{\phi}}_I^{n_M}(r_N,\theta_N) & \bar{\boldsymbol{\phi}}_{II}^{n_m}(r_N,\theta_N) & \dots & \bar{\boldsymbol{\phi}}_{II}^{n_M}(r_N,\theta_N) \end{pmatrix}. \tag{6}$$

In this equation, i_o is the index of the first node in the extraction domain which contains all the nodes with an index between i_o and N. Using this description, the $2(i_o-1)$ first degrees of freedom in $\mathbf{U}_r$ are standard finite element degrees of freedom but the $2N_w$ last degrees of freedom correspond to the amplitude of the N_W functions for mode I and

Prepared using nmeauth.cls DOI: 10.1002/nme

mode *II*:

$$\mathbf{U}_r = \begin{bmatrix} u_1 \\ \vdots \\ u_{2(i_o-1)} \\ a_I^{n_m} \\ \vdots \\ a_I^{n_M} \\ a_{II}^{n_m} \\ \vdots \\ a_{II}^{n_M} \end{bmatrix}. \tag{7}$$

2.3. Mesh adaptation

The Williams' expansion is written in a polar coordinate system. It is thus convenient to use this description over a circular domain. The finite element mesh is thus adapted to have an explicit description of a circle of radius r_{tip} centered at the crack tip (see Figure 1). The nodes along the crack path are split to allow displacement discontinuity across the crack faces. For using the first super-singular Williams' component to detect the crack tip position along the crack faces (see Section 4.2), it is required that a small disc around the crack tip is discarded from the analysis. The finite element mesh thus also explicitly describes a circle of radius r_{int}. The elements inside this circle are removed from the initial finite element mesh. The element size is refined in the extraction domain Ω_K to control the interpolation error between the finite element description and the analytical Williams' functions in the condensation operator. A factor of 10 between the element size and the radius of the extraction domain r_{tip} has shown, in the present work, to be a good compromise between accuracy and computational cost.

Prepared using nmeauth.cls
DOI: 10.1002/nme

3. DIGITAL IMAGE CORRELATION

To follow crack propagation, a series of digital images is captured and then analyzed. However, at each step (image), the analysis reduces to the study of a pair of images: f, the reference image associated with the reference state of the structure, and g namely the deformed image associated with the deformed state. A matrix-vector format is also adopted for the images data. For an image f, $\mathbf{F}$ is a column vector that contains the grey level of each pixel in the area covered by the mesh. Within this formalism, the pixel integration (discrete summation over the pixels) simply writes as a scalar product between two column vectors.

3.1. Optical flow

The optical flow equation states that the grey level variation between the reference state f and the deformed state g is due to only the passive (no source term) advection of image texture (the grey level is an intrinsic property of a material point):

$$f(\mathbf{X_p}) = g(\mathbf{X_p} + \mathbf{u}(\mathbf{X_p})), \tag{8}$$

$\mathbf{X_p}$ giving the position of a pixel in the global coordinate system. A non-linear least-squares resolution scheme of this equation adopted in the following [25]. After the finite element discretization of the displacement has been introduced and the equation is linearized with respect to the solution increment $\mathrm{d}\mathbf{U} = \mathbf{U} - \mathbf{U}^p$, where $\mathbf{U}^p$ is the solution at the previous iteration, a linear system is obtained:

$$[\mathbf{M}]\ \{\mathrm{d}\mathbf{U}\} = \{\mathbf{b}\}. \tag{9}$$

In this equation, the following expression is adopted for $\mathbf{M}$:

$$[\mathbf{M}] = [\mathbf{N}]^T [\nabla \mathbf{F}] [\nabla \mathbf{F}] [\mathbf{N}], \tag{10}$$

and $\mathbf{b}$ is given by

$$\{\mathbf{b}\} = [\mathbf{N}]^T [\nabla \mathbf{F}] \{\mathbf{F} - \mathbf{G}\} \tag{11}$$

Prepared using nmeauth.cls
DOI: 10.1002/nme

In these equation $\nabla\mathbf{F}$ is the vector containing the values of the image gradient , computed by a central finite difference method, at each pixel.

3.2. Elastic regularization

To compensate for the use of a small extraction domain, an elastic regularization of the optical flow is adopted. Let $\mathbf{K}$ be the elastic finite element stiffness matrix calculated for the adapted mesh, then Equation (9) is augmented by adding a weighted equilibrium gap energy [26]

$$\left([\mathbf{M}]+\omega(\ell_c)\,[\mathbf{K}]^T\,[\mathbf{P}]^T\,[\mathbf{P}]\,[\mathbf{K}]\right)\,\{\mathbf{U}\}=\{\mathbf{b}\}+[\mathbf{M}]\,\{\mathbf{U}^p\}. \tag{12}$$

In this equation, $\omega(\ell_c)$ is a scalar parameter weighting the regularization. It has been shown that the regularization introduces a mechanical low-pass filter which cut-off wave length ℓ_c can be controlled [27]. $\mathbf{P}$ is a selection matrix that allows to select the DOF to be controlled by the elastic regularization. It formally reads as a diagonal matrix with 1 if the corresponding degree of freedom is regularized, and 0 if not. In the present case the degrees of freedom hold by the nodes inside the extraction domain Ω_K are not regularized as they are constrained by the condensation operator $\mathbf{L}$ that intrinsically prescribes divergence free elastic stress. The nodes on the boundary of the structure that are submitted to non stress free conditions are not regularized as well (see Figure 1). This system is solved very efficiently with a preconditioned conjugate gradient solver using $\mathbf{U}^p$ as an initial solution. The convergence is typically reached within 3 to 5 iterations.

Using the condensation, the resolution algorithm is written in term of $\mathbf{U}_r$ by introducing Equation (5) into Equation (12):

$$[\mathbf{L}]^T\left([\mathbf{M}]+\omega(\ell_c)\,[\mathbf{K}]^T\,[\mathbf{P}]^T\,[\mathbf{P}]\,[\mathbf{K}]\right)[\mathbf{L}]\,\{\mathbf{U}_r\}=[\mathbf{L}]^T\,\{\mathbf{b}\}+[\mathbf{L}]^T\,[\mathbf{M}]\,[\mathbf{L}]\,\{\mathbf{U}_r^p\}. \tag{13}$$

After convergence is reached, the resolution directly provides estimates of the selected Williams' amplitudes a_j^n. They are then scaled to obtain the meaningful quantities as SIF

DOI: 10.1002/nme

or T-stress:

$$K_I = 2\mu\sqrt{2\pi}\, a_I^1, \qquad K_{II} = 2\mu\sqrt{2\pi}\, a_{II}^1, \qquad T = 2\mu\sqrt{2\pi}\, a_I^2, \tag{14}$$

where μ is the first Lamé constant given by $\mu = \frac{E}{2(1+\nu)}$, E being the Young's modulus.

4. IMPLEMENTATION

In this section, all the steps required to obtain the crack path, crack tip position and SIF estimates are detailed. A graphical overview of the methodology is presented in Figure 2.

4.1. Crack path detection

As proposed in [28], the correlation residual map $\eta = |f(\mathbf{X_p}) - g(\mathbf{X_p} + \mathbf{u}(\mathbf{X_p}))|$ allows for a robust positioning of the crack surface. This was used in 2D but also in 3D *e.g.* [9, 7]. The crack surface is defined from the residual map either manually or automatically by tracking the surface of maximum error [28, 9] or using a virtual image correlation technique [29, 30]. To get a residual map η suitable for using one of these detection algorithms, a displacement measurement analysis is run for all the images of the experiment using a non-conforming regular mesh. Since the displacement discontinuity at the crack faces are not described, large error levels are obtained on the crack faces.

After the crack surface detection is performed, either for a set of points or a level set function, a mesh adapted to the sample boundaries and the crack faces is generated. It also fulfills the requirements for direct SIF estimation using the condensation method proposed above (explicit description of a circle of radius r_{tip} to define the extraction domain and a circle of radius r_{int} for element removal).

4.2. Crack tip detection

Once the crack surface is defined, the crack tip position is tracked along the crack support. The image sequence is analyzed starting from the last state using the adapted

Prepared using nmeauth.cls
DOI: 10.1002/nme

mesh and direct SIF estimation. The Williams' expansion is truncated between $n_m = -3$ and $n_M = 7$. Super-singular terms are used following [20]. The $n = -1$ term can be used to detect the equivalent elastic crack tip position. For this purpose, the following property of Williams' functions is used:

$$\frac{\partial \boldsymbol{\phi}_j^n}{\partial x} = \frac{n}{2}\boldsymbol{\phi}_j^{n-2}. \tag{15}$$

Then, suppose that the estimated crack tip position is shifted by a small distance d. If the displacement $\boldsymbol{u}_w$ is expressed as a function of the Williams' series in the shifted coordinate system ($\tilde{z} = z + d$)

$$\boldsymbol{u}_w = \sum_{n\geq 0,j} a_j^n \boldsymbol{\phi}_j^n(z) = \sum_{n,j} \tilde{a}_j^n \boldsymbol{\phi}_j^n(\tilde{z}), \tag{16}$$

using a first order Taylor expansion of $\boldsymbol{\phi}_j^n(\tilde{z})$ and Equation (15) allows consideration of not only $n \geq 0$ terms but also $n < 0$ terms. Then, one can write the following by considering that the expression of $\boldsymbol{u}_w$ from Equation 4 has a zero term for $n = -1$ and mode I:

$$-\frac{d}{2}\tilde{a}_I^1 + \tilde{a}_I^{-1} = 0. \tag{17}$$

The crack tip position along the crack faces and coordinate system is progressively corrected until sufficient precision (for the crack tip position) is reached. Because the first order correction only is considered in order to obtain Equation 17, the relation between the actual shift, d, and its estimation from $-2\tilde{a}_I^{-1}/\tilde{a}_I^1$ is linear. In practice, this linear dependence is observed to occur for quite a large range of crack tip shifts and convergence is usually obtained in 2 or 3 iterations.

To avoid expensive computational cost due to remeshing, a mesh morphing technique is used to update the mesh between two iterations of the crack tip detection. An elastic finite element simulation, with 0 Poisson's ratio, is run under the following boundary conditions:

- all the nodes inside the extraction domain have a prescribed displacement of d along the local tangent to the crack tip x,

Prepared using nmeauth.cls DOI: 10.1002/nme

- the displacement of the nodes on the crack faces (except those inside the extraction domain) is along the local tangent to the crack surface only,
- the non-regularized nodes on the mesh boundary are fixed,
- the displacement of all the other nodes on the mesh boundary is along the local tangent to the mesh boundary only.

Once convergence is reached on the crack tip position, *i.e.* the correction d being lower than 1 pixel in amplitude, the values of the meaningful Williams' amplitudes are stored as well as the position of the crack tip. Then, a new mesh is generated and the previous image is analyzed. This avoids large mesh distortion and preserves computational cost.

The performance of the proposed methodology will now be evaluated for two examples. Especially, it will be assessed that small extraction domains can be used with the proposed strategy because the elastic regularization preserves from increasing uncertainty on the SIF and estimated crack tip position.

5. EXAMPLES

The method proposed in the present paper is now tested with two examples. The first example is based on the analysis of artificially deformed images. As the crack tip position and SIF amplitudes are prescribed, this example allows for a quantitative evaluation of the performance of the method. Then the ability of the method to track curved crack paths is illustrated through the analysis of an experiment.

5.1. Synthetic images analysis

Starting from a real 128×128 pixels image duplicated four times in each direction (see Figure 3(a)), a series of 7 1024×1024 pixels images is generated. For generating these images, the same sub-pixel grey level interpolation as for digital image correlation is used, *i.e.* cubic splineinterpolation. The displacement field used to deforme the reference image consists of a mode I singular field, $n = 1$. The amplitude a_I^1 of the prefactor of

Prepared using nmeauth.cls DOI: 10.1002/nme

$\boldsymbol{\phi}_I^1$ is set so that the maximum displacement jump is 1.25 pixel. The Poisson's ratio is 0.3 and the Young's modulus 210 GPa. Plane strain condition is assumed. The crack is aligned with the vertical axis, it is centered with respect to the horizontal axis and the crack tip position varies from -10 pixels to 50 pixels by steps of 10 pixels from the image center.

A square region of 530×530 pixels centered in the reference image is analyzed. The background element size is 30 pixels. The influence of the extraction domain size r_{tip} (varying between 30 and 100 pixels) and the influence of the cut-off wave length of the elastic regularization ℓ_c (varying from 0 to 400 pixels) are analyzed. Inside the extraction domain the ratio between the extraction radius and the element size is set to 10. r_{int} is set to 20 pixels. In this analysis, the crack position is fixed but the crack tip position is searched for.

A example analysis is obtained for $\ell_c = 400$ pixels and $r_{tip} = 40$ pixels. Figure 3(b) shows the mesh used for this analysis and Figures 3(c) and 3(d) the horizontal and vertical displacement fields for the last image. The SIF and crack tip position history are compared to the prescribed values on Figure 4. A good agreement between the values estimated by this example analysis and the prescribed values is obtained. A more quantitative insight into the performances of the method is given below. Two error indicators are used for this purpose:

- the RMS relative SIF error that is calculated by taking the standard deviation (RMS) over the propagation steps of the relative gap in SIF (the scatter between the estimated value and the prescribed one normalized by the prescribed value)
- the RMS crack tip position error that is calculated by taking the standard deviation over the propagation steps of the gap between the estimated crack tip position and the prescribed one.

Prepared using nmeauth.cls
DOI: 10.1002/nme

These indicators allow for quantifying the uncertainty on these two output variables (SIF and crack tip position) of the analysis. The evolution of these indicators with respect to ℓ_c and r_{tip} is detailed below.

Influence of r_{tip} For these analyses, ℓ_c is set to 400 pixels but r_{tip} is varying between 30 and 100 pixels. Analyses are also conducted with the integrated approach in [5]. They are labelled as W-DIC. These analyses were carried out to show how the uncertainty increases when the extraction radius is decreasing. Indeed, in Figure 5, it is observed that the uncertainty of W-DIC analyses exponentially increases when r_{tip} is decreasing. Conversely, thanks to the elastic regularization, the extraction radius does not influence the results obtained by the proposed method. The averaged RMS relative SIF error is about 1.5×10^{-3} and the average RMS crack tip position error is about 0.5 pixel. Note that the convergence criterion for crack tip detection is set to 1 pixel. The error obtained for these analyzes on synthetic images should have been lower with a lower convergence criterion. However, a value lower than 1 pixel may be unrealistic for the real experimental case.

This first series of analyses shows that a very small extraction domain size can be used without deteriorating the performances of the method. Indeed, the elastic regularization allows the outer domain (outside the extraction domain) to share far-field information with the analytical model whatever the extraction domain size, thus keeping the uncertainty levels very low. The key parameter thus seems to be the cut-off wave length ℓ_c.

Influence of ℓ_c The extraction domain size is now kept at 40 pixels and ℓ_c is varying from 0 to 400 pixels. The case $\ell_c = 0$ pixel corresponds to the integrated method W-DIC [5]. The evolution of the error indicators is shown in Figure 6. Concerning the crack tip positioning, it is obtained that the elastic regularization is very efficient, meaning that even for low values of ℓ_c (from 10 pixels), the uncertainty is lower than or about 1 pixel.

Prepared using nmeauth.cls
DOI: 10.1002/nme

For the SIF, the evolution of uncertainty with the cut-off wave length is also sharp and an improvement of the sensitivity is obtained when increasing ℓ_c. A fit, on a power law, in a logarithmic scale gives a slope of -1 meaning that the SIF uncertainty behaves as $1/\ell_c$.

From these two series of analyzes, it is concluded that the proposed method with direct SIF estimation by condensation and elastic regularization allows for estimating SIF and crack tip position even for small extraction domains. The extraction domain can be as small as required by the crack curvature provided there is a layer of about 10 elements along its radius and the cut-off wave length of the elastic regularization is about the extraction domain size.

5.2. Mixed mode crack propagation experiment

An experiment is conducted using a conventional tensile electromechanical device. The geometry of the sample, inspired from [31], is a rectangular plate of 140 mm$\times$70 mm with a hole of 30 mm in diameter, see Figure 7. The hole center is aligned along the transverse (Y) direction and it is shifted by 25 mm from the specimen center along X direction. The specimen thickness is 10 mm, leading to an approximation of the 3D state by a 2D plane strain hypothesis. The material is a commercial PolyMethyl Methacrylate (PMMA) (Perspex). Its elastic properties, within the strain rate range of the quasi-static experiment conducted herein, are taken to $E = 5GPa$ for the Young's modulus and $\nu = 0.32$ for the Poisson's ratio.

A pre-notch is machined manually before the specimen is submitted to a compressive load along X at a constant speed of 0.1 mm/min. The pre-notch of about 35 mm length from the hole center, with an angle of 30^o with respect to the X axis, is chosen for generating mixed-mode conditions at initiation and growth. It is expected that the crack runs along X and progressively reaches the specimen axis, leading to a pure mode I situation.

Prepared using nmeauth.cls
DOI: 10.1002/nme

During the experiment, grey scale images of 4872×3248 pixels, with 8-bit digitization, are acquired. The camera is mounted with a 200 mm Nikon lens, resulting in a physical pixel size of 32.5 μm. The sample surface is prepared using white and black spray paints, see Figure 7. 113 images are captured before complete failure. Crack initiation occurs at images number 27. In the results presented below, the time scale is shifted so that crack initiation occurs at t=0. The time is in fact a virtual time standing for the image number.

First, an analysis with a regular mesh of quadrangular elements of 64-pixel side is performed. The two components of the displacement field for the last image are displayed in Figure 8. The discontinuity of the displacement field across the crack faces is clearly evidenced for the two displacement components, unlike it is smoothed by the regular finite element mesh. Crack openings of about 20 pixels are obtained at this loading step. From this analysis, an correlation error map η is computed and then used to determine the crack path as shown in Figure 9. In this Figure, the detected crack path is super-imposed to the element-wise average of η and to the reconstructed pixel map of η. This crack path geometry is now used to generate adapted meshes to track the crack tip position using the method proposed in this paper. For generating these meshes, the background element size is 64 pixels. The extraction domain size is $r_{tip} = 64$ pixels and the element size in the extraction domain is set to 8 pixels while the element size along the crack faces is fixed to 32 pixels. The cut-off wave length ℓ_c of the elastic regularization is set to 256 pixels. An example mesh is shown in Figure 7(b) where the extraction domain boundary and crack path are plotted in red. The initiation phase and the propagation phase are further analyzed below.

5.2.1. Initiation Images for time from -8 to 0 are analyzed in this paragraph. The crack tip position is searched for along the machined pre-notch. The displacement field at time 0 is plotted in Figure 10. Thanks to the adapted mesh, the displacement discontinuity across the crack faces is now explicitly captured. For illustration purposes,

Prepared using nmeauth.cls DOI: 10.1002/nme

the displacement field used to deform the mesh, avoiding remeshing at each step of the iterative search of the crack tip position, is plotted in Figure 11. The boundary conditions (see Section 4.2) used to generate this field are clearly observed. The experimental configuration (loading and sample geometry), leading to mixed-mode situation as evidenced by the discontinuity of the two components of the displacement, is further illustrated by the SIF plot in Figure 12. The results in this Figure show a predominant mode II, K_{II} being about one order of magnitude higher than K_I in amplitude. In *Figure* 12, negative values of K_I are reported. These negative values correspond to a globally compressive loading of the specimen and they are allowed by the non-zero finite thickness of the machined pre-notch. Indeed, crack faces are allowed to *close* due to the pre-notch thickness resulting in negative K_I values. The equivalent mode I SIF K_{Ieq}, in the sense of the maximum hoop stress, is also plotted in Figure 12. A values of K_{Ieq} at initiation is 2.23 MPa.m$^{1/2}$. After this initiation phase, the crack starts propagating with a kink due to the high mode mixity of the loading. The propagation phase is analyzed below.

5.2.2. Propagation For the propagation phase, images corresponding to time 1 until 85 are analyzed. The crack tip is searched for along the crack path shown in Figure 9. The displacement field for the last analyzed image is displayed in Figure 13. Again, the adapted mesh, as shown in Figure 7(b), allows for capturing the displacement discontinuity. A close view of the crack tip field during crack propagation is depicted in Figure 14 where the deformed mesh is plotted on the deformed image. Contrary to the initiation phase, along the end of the crack path which is close to align with the X axis, the X component of the displacement shows no discontinuity. Conversely, the Y component is discontinuous, illustrating a predominantly mode I situation. This is confirmed in Figure 15 which shows the evolution of the SIF and T-stress during crack propagation, the latter being directly estimated within the Williams' formalism. K_I is about 10 times higher than K_{II} in amplitude. Higher mode mixity is obtained just after

Prepared using nmeauth.cls DOI: 10.1002/nme

initiation and it changes sign during propagation. However, the values for K_{II} are very low in amplitude and this is difficult to interpret. The values of K_{Ieq} just after initiation are slightly lower than the value obtained at initiation. This is due to the finite thickness of the pre-notch that leads to a lower singularity and thus an estimated value for K_{Ieq} at initiation higher than the one produced by a sharp crack. Then the value of K_{Ieq} is slightly decreasing as the crack propagates. This should be linked to the variation in the crack tip speed as obtained in Figure 16 but also to the variation of the T-stress induced by structural effects as observed in Figure 15.

6. CONCLUSION

In this paper, a methodology is proposed to experimentally estimate crack tip position and SIF along curved crack paths using digital images. The method is based on a digital image correlation technique using finite elements with mesh adaptation and a truncated Williams' expansion. The two descriptions are coupled through a condensation of the finite element degrees of freedom onto the Williams' coefficients. The analysis of a curved crack path requires a small extraction domain compared to the crack curvature. The decrease of the robustness of the extraction of the crack tip position and the SIF is compensated herein by using an elastic regularization over the finite element adapted mesh. It is shown by the first example in the paper, that the robustness of the proposed methodology does not depend on the extraction domain size, which can thus be chosen as small as required by the crack curvature, but on the cut-off wave length of the elastic regularization. However, a cut-off wave length of the order of the extraction domain size ensures robust extraction of crack tip position and SIF. The ability of the proposed methodology to track curved cracks is then illustrated through the analysis of an experiment. Initiation and crack propagation are analyzed and robust estimates of SIF, T-stress and crack length are obtained. A fast and complete implementation of the

Prepared using nmeauth.cls
DOI: 10.1002/nme

method is also detailed in the paper. Compared to direct finite element simulations of the experiment, the approach proposed in the paper offers the following capabilities:

i in the proposed strategy, there is no need for boundary conditions other than stress free conditions. The biases that may be introduced by considering idealized, Dirichlet or non-zero Neumann, conditions are thus avoided. This problem was already emphasized in the literature for 3D stationary cracks [32] or for the identification of material parameters [33].

ii performing a finite element simulation of crack propagation requires a criterion for the crack angle and a crack growth law. Concerning the crack angle, the max hoop stress criterion has shown its ability to capture the crack bifurcation in a *brittle* material such PMMA. Common pratices for crack growth are to suppose that the crack propagates at a constant value of K_{Ieq}, or to adopt a Paris' like regularization of the Griffith's law. It is clearly shown by the results of this paper that, for the analyzed case, the relation between K_{Ieq} and the crack tip velocity is much more complex. In Figure 15, it is observed that K_{Ieq} starts decreasing from step 50 whereas it is observed on Figure 16 that the crack is accelerating from this step. This point was not emphasized in this paper for which the focus is kept on the technical aspects. However, the results presented (which are probably among the first ones for a curved crack) migh open a discussion *e.g.* on the effect of the crack curvature or of the T-stress on the crack velocity.

Prepared using nmeauth.cls DOI: 10.1002/nme

REFERENCES

1. Duarte C, Hamzeh O, Liska T, Tworzydlo W. A generalized finite element method for the simulation of three-dimensional dynamic crack propagation. *Computer Methods in Applied Mechanics and Engineering* 2001; **190**:2227–2262.
2. McNeill S, Peters W, Sutton M. Estimation of stress intensity factor by digital image correlation. *Engineering Fracture Mechanics* 1987; **28**(1):101–112.
3. Abanto-Bueno J, Lambros J. Investigation of crack growth in functionally graded materials using digital image correlation. *Engineering Fracture Mechanics* 2002; **69**:1695–1711.
4. Yoneyama S, Morimoto Y, Takashi M. Automatic evaluation of mixed-mode stress intensity factors utilizing digital image correlation. *Strain* 2006; **42**:21–29.
5. Roux S, Hild F. Stress intensity factor measurement from digital image correlation: post-processing and integrated approaches. *International Journal of Fracture* 2006; **140**(1-4):141–157.
6. Lopez-Crespo P, Burguete R, Patterson E, Shterenlikht A, Withers P, Yates J. Study of a crack at a fastener hole by digital image correlation. *Experimental mechanics* 2009; **49**(4):551–559.
7. Réthoré J, Limodin N, Buffière JY, Hild F, Ludwig W, Roux S. Digital volume correlation analyses of synchrotron tomographic images. *Journal of Strain Analysis for Engineering Design* 2011; **46**:683–695.
8. Réthoré J, Gravouil A, Morestin F, Combescure A. Estimation of mixed-mode stress intensity factors using digital image correlation and an interaction integral. *International Journal of Fracture* 2005; **132**(1):65–79.
9. Rannou J, Limodin N, Réthoré J, Gravouil A, Ludwig W, Baietto-Dubourg MC, Buffière JY, Combescure A, Hild F, Roux S. Three dimensional experimental and numerical analysis of a fatigue crack. *Computer Methods in Applied Mechanics and Engineering* 2009; **99**(1-2):1307–1325, doi: 10.1016/j.cma.2009.09.013.
10. Réthoré J, Roux S, Hild F. Noise-robust stress intensity factor determination from kinematic field measurements. *Engineering Fracture Mechanics* 2008; **75**(13):3763–3781.
11. Réthoré J, Roux S, Hild F. Optimal and noise-robust extraction of fracture mechanics parameters from kinematic measurements. *Engineering Fracture Mechanics* 2011; **78**(9):1827–1845.
12. Liu XY, Xiao QZ, Karihaloo BL. Xfem for direct evaluation of mixed mode sifs in homogeneous and bi-materials. *International Journal for Numerical Methods in Engineering* 2004; **59**:1103–1118.
13. Chahine E, Laborde P, Renard Y. Crack-tip enrichment in the xfem method using a cut-off function. *International Journal for Numerical Methods in Engineering* 2008; **75**(6):629–646.
14. Xiao Q, Karihaloo B. Implementation of hybrid crack element on a general finite element mesh and in combination with xfem. *Computer methods in applied mechanics and engineering* 2007; **196**(13):1864–1873.

Prepared using nmeauth.cls DOI: 10.1002/nme

15. Réthoré J, Roux S, Hild F. Hybrid analytical and extended finite element method (HAX-FEM): A new enrichment procedure for cracked solids. *International Journal for Numerical Methods in Engineering* 2010; **81**(3):269–285, doi:10.1002/nme.2691.
16. Passieux J, Gravouil A, Réthoré J, Baietto MC. Direct estimation of generalized stress intensity factors using a three-scale concurrent multigrid x-fem. *International Journal for Numerical Methods in Engineering* 2010; **85**(13):1648–1666, doi:10.1002/nme.3037.
17. Williams M. On the stress distribution at the base of a stationary crack. *ASME Journal Applied Mechanics* 1957; **24**:109–114.
18. Réthoré J, Roux S, Hild F. Mixed-mode crack propagation using a hybrid analytical and extended finite element method. *Comptes rendus - Mécanique* 2010; **338**:121–126, doi:10.1016/j.crme.2010.03.001.
19. Passieux J, Réthoré J, Gravouil A, Baietto MC. Local/global non-intrusive crack propagation simulation. *Computational Mechanics* 2013; **52**:1381–1393.
20. Hammam R, Hild F, Roux S. Stress intensity factor gauging by digital image correlation: Application in cyclic fatigue. *Strain* 2006; **43**(3):181–192.
21. Henninger C, Roux S, Hild F. Enriched kinematic fields of cracked structures. *International Journal of Solids and Structures* 2010; **47**(24):3305–3316.
22. Leplay P, Réthoré J, Meille S, Baietto MC. Identification of damage and cracking behaviours based on energy dissipation mode analysis in a quasi-brittle material using digital image correlation. *International Journal of Fracture* 2011; **171**(1):35–50.
23. Réthoré J, Estevez R. Identification of a cohesive zone model from digital images at the micron-scale. *Journal of the Mechanics and Physics of Solids* 2013; **61**(6):1407–1420.
24. Durif E, Réthoré J, Combescure A, Fregonese M, Chaudet P. Controlling stress intensity factors during a fatigue crack propagation using digital image correlation and a load shedding procedure. *Experimental Mechanics* 2011; .
25. Besnard G, Hild F, Roux S. 'finite-element' displacement fields analysis from digital images: Application to Portevin-Le Châtelier bands. *Experimental Mechanics* 2006; **46**(6):789–803.
26. Réthoré J, Hild F, Roux S. An extended and integrated digital image correlation technique applied to the analysis of fractured samples. *European Journal of Computational Mechanics* 2009; **18**:285–306.
27. Leclerc H, Périé JN, Hild F, Roux S. Digital volume correlation: what are the limits to the spatial resolution? *Mechanics & Industry* 2012; **13**(06):361–371.
28. Réthoré J, Hild F, Roux S. Extended digital image correlation with crack shape optimization. *International Journal for Numerical Methods in Engineering* 2008; **73**(2):248–272, doi:10.1002/nme.2070.
29. Réthoré J, François M. Curve and boundaries measurement using b-splines and virtual images. *Optics and Lasers in Engineering* 2014; **52**:145–155.

30. Lachambre J, Réthoré J, Weck A, Buffiere J. Extraction of stress intensity factors for 3d small fatigue cracks using digital volume correlation and x-ray tomography. *International Journal of Fatigue* 2015; **71**:3–10.

31. Grégoire D, Maigre H, Réthoré J, Combescure A. Dynamic crack propagation under mixed-mode loading - comparison between experiments and x-fem simulations. *International Journal of Solids and Structures* 2007; **44**(20):6517–6534, doi:10.1016/j.ijsolstr.2007.02.044.

32. Roux S, Réthoré J, Hild F. Digital image correlation and fracture: an advanced technique for estimating stress intensity factors of 2d and 3d cracks. *Journal of Physics D: Applied Physics* 2009; **42**(214004), doi:10.1088/0022-3727/42/21/214004.

33. Réthoré J. A fully integrated noise robust strategy for the identification of constitutive laws from digital images. *International Journal for Numerical Methods in Engineering* 2010; **84**:631–660, doi: 10.1002/nme.2908.

Prepared using nmeauth.cls
DOI: 10.1002/nme

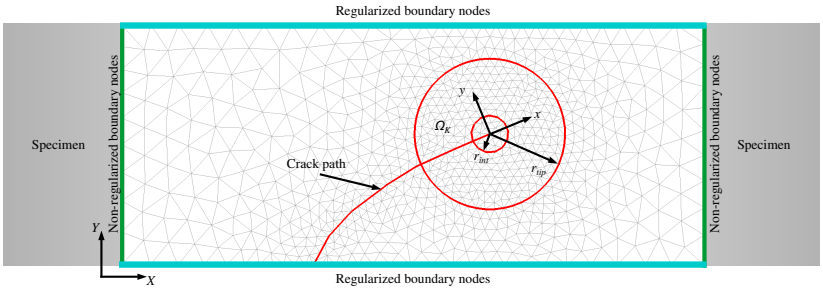

Figure 1. Shematic representation of a sample with a crack. Definition of: the global coordinate system (X,Y), the local coordinate system (x,y), the extraction domain Ω_K and its radius r_{tip} and the radius r_{int} of the zone of removed elements at the crack tip.

Prepared using nmeauth.cls
DOI: 10.1002/nme

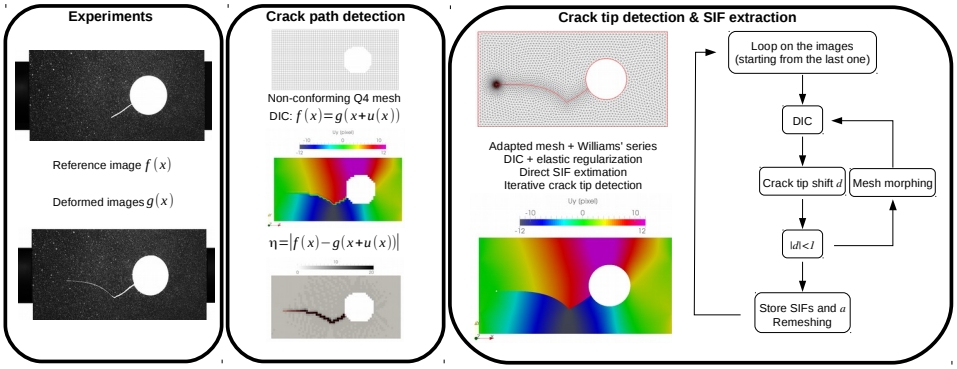

Figure 2. Overview of the main steps of the proposed methodology: crack path detection and crack tip detection with SIF extraction.

Prepared using nmeauth.cls
DOI: 10.1002/nme

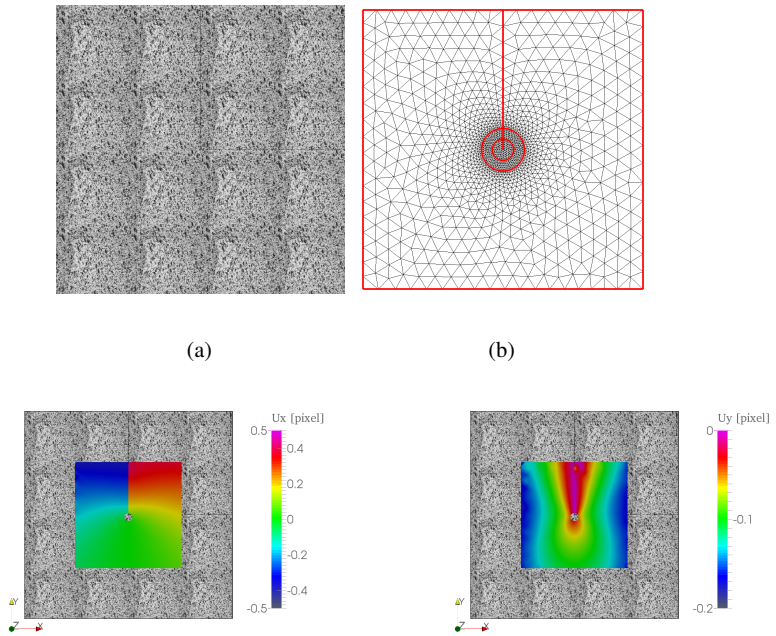

(a) (b)

(c) (d)

Figure 3. Reference image for the synthetic image example (a), an example mesh with $r_{tip} = 40$, $h = 4$ and $\ell_c = 400$ (b). The horizontal and vertical displacement field in pixel for the last image of the series are plotted on sub-figures (c) and (d).

Prepared using nmeauth.cls
DOI: 10.1002/nme

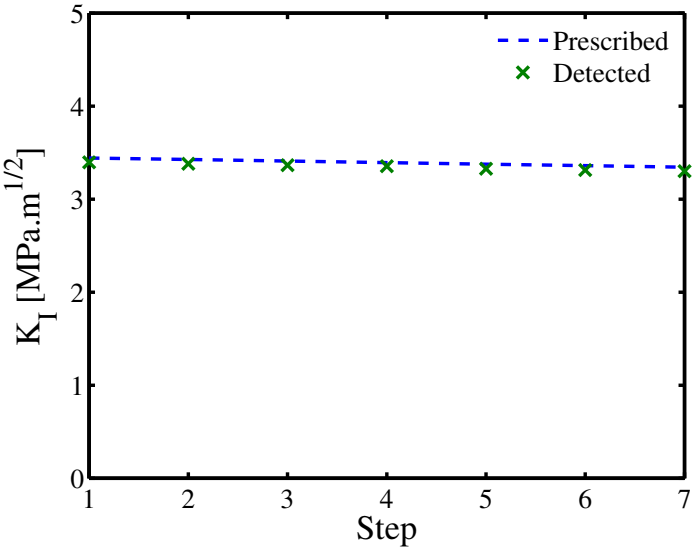

(a)

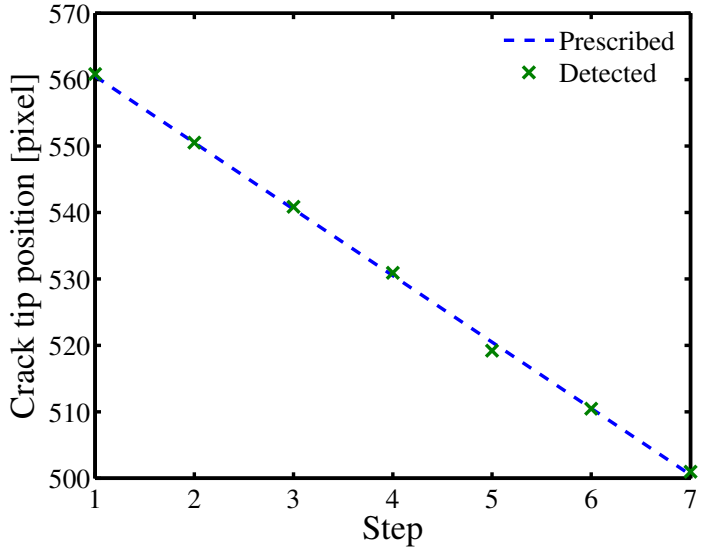

(b)

Figure 4. SIF (a) and crack tip position (b) obtained for $r_{tip} = 40$, $h = 4$ and $\ell_c = 400$, compared to the prescribed solution.

Prepared using nmeauth.cls
DOI: 10.1002/nme

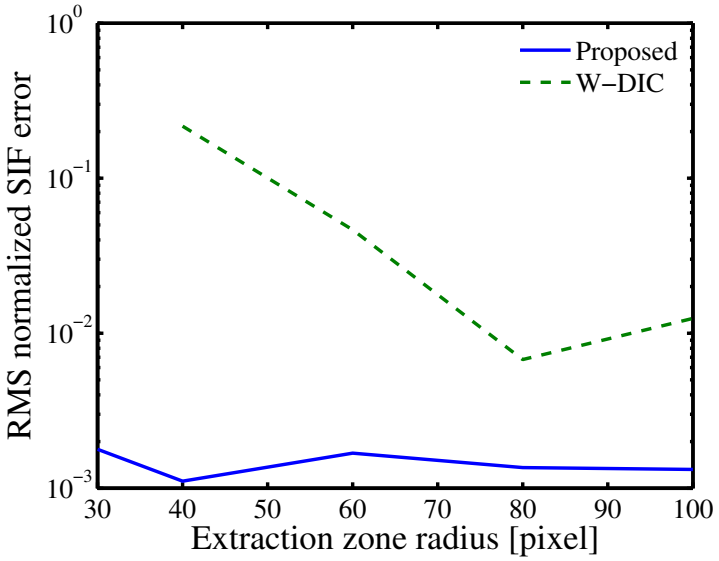

(a)

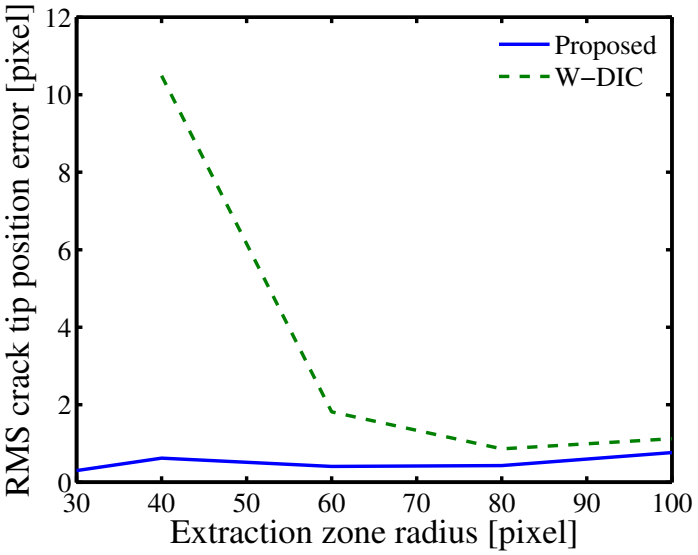

(b)

Figure 5. Relative RMS SIF error and RMS crack tip position error as a function of the extraction domain size for the proposed method and the integrated method (W-DIC) in [5].

Prepared using nmeauth.cls
DOI: 10.1002/nme

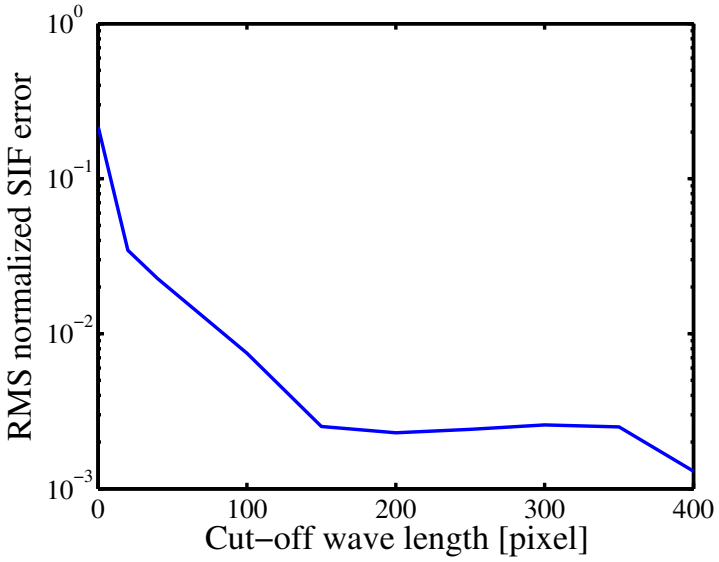

(a)

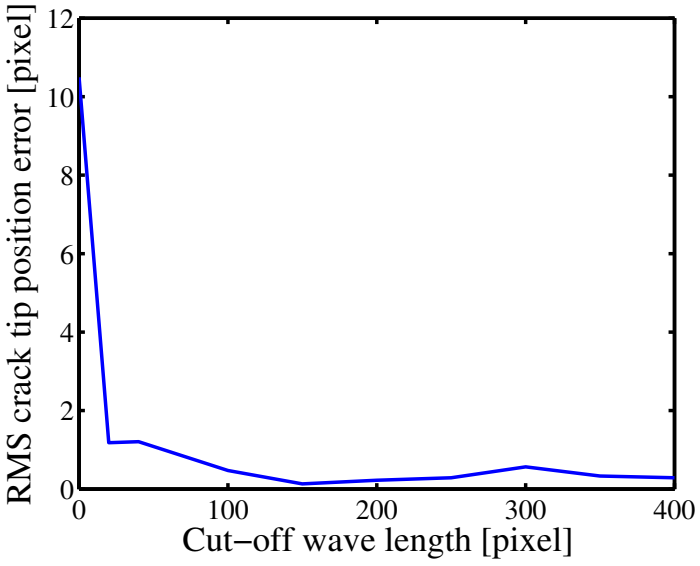

(b)

Figure 6. Relative RMS SIF error and RMS crack tip position error as a function of the cut-off wave length ℓ_c of the elastic regularization.

Prepared using nmeauth.cls
DOI: 10.1002/nme

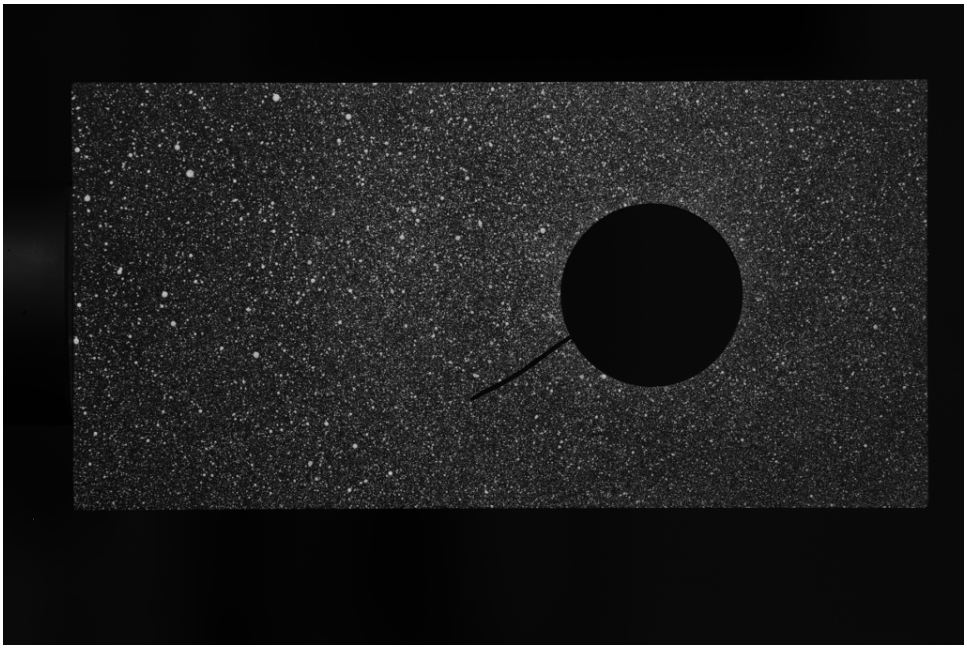

(a)

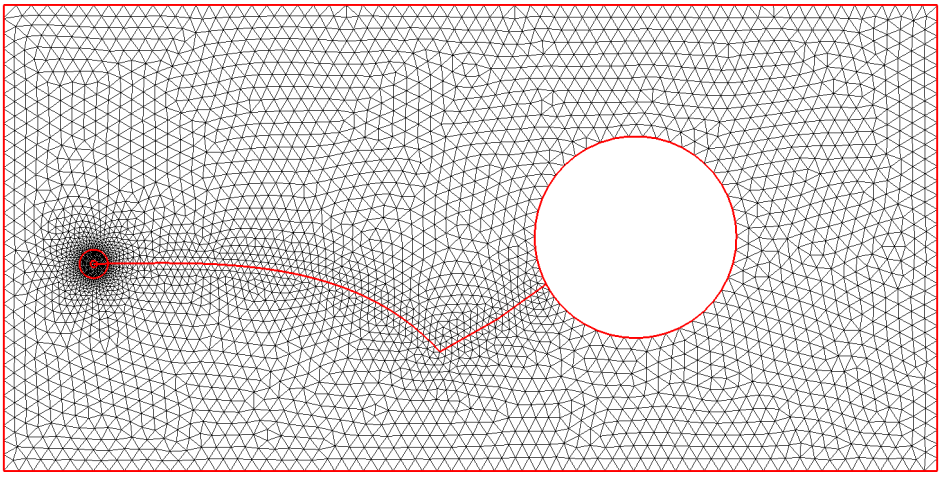

(b)

Figure 7. Reference image (a) and example mesh (b) for the experiment.

Prepared using nmeauth.cls
DOI: 10.1002/nme

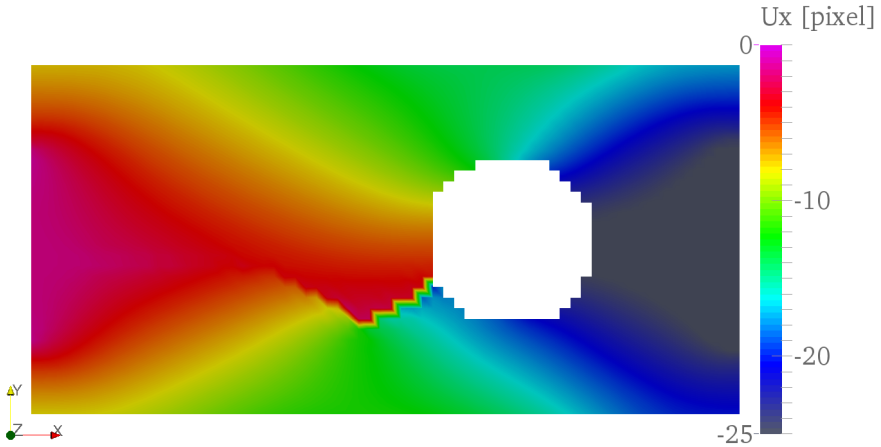

(a)

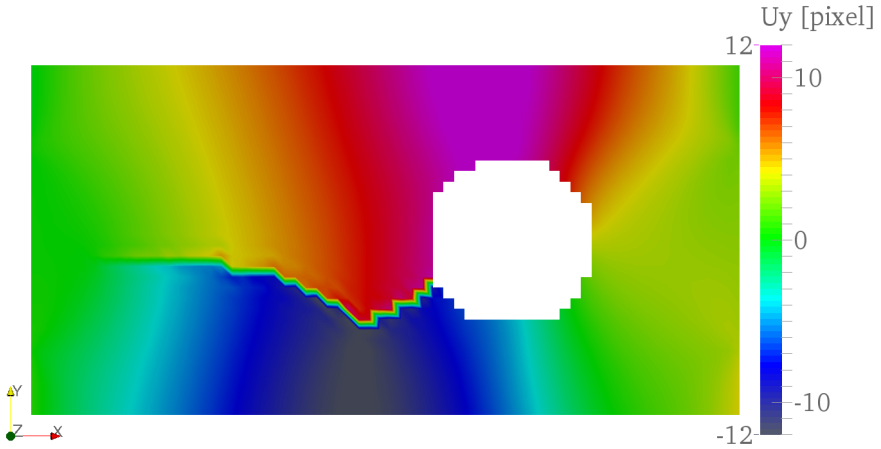

(b)

Figure 8. Horizontal and vertical displacement map (in pixel) for the last image and a regular finite element mesh with 64-pixel elements.

Prepared using nmeauth.cls
DOI: 10.1002/nme

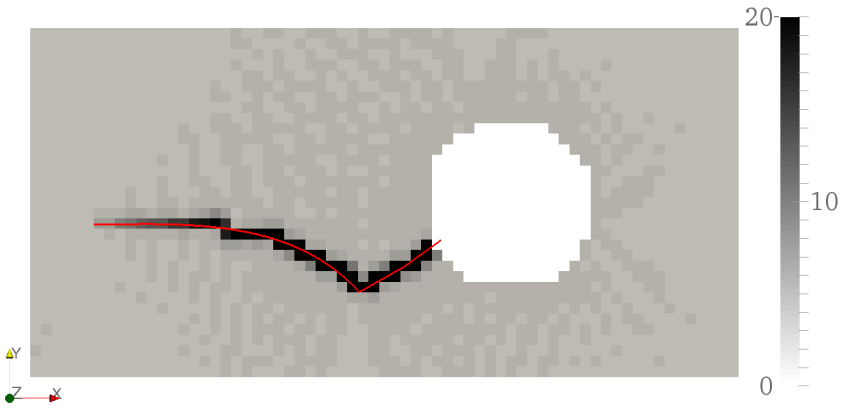

(a)

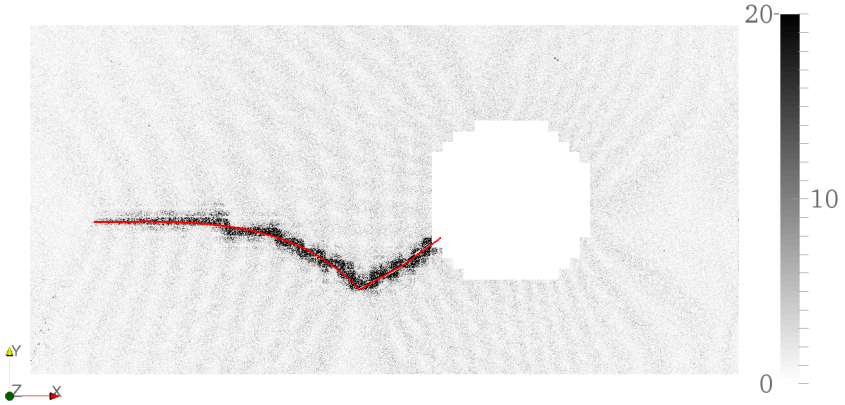

(b)

Figure 9. Correlation error map for the last image and a regular finite element mesh with 64-pixel elements. (a) element average error and (b) pixel map in grey level.

Prepared using nmeauth.cls
DOI: 10.1002/nme

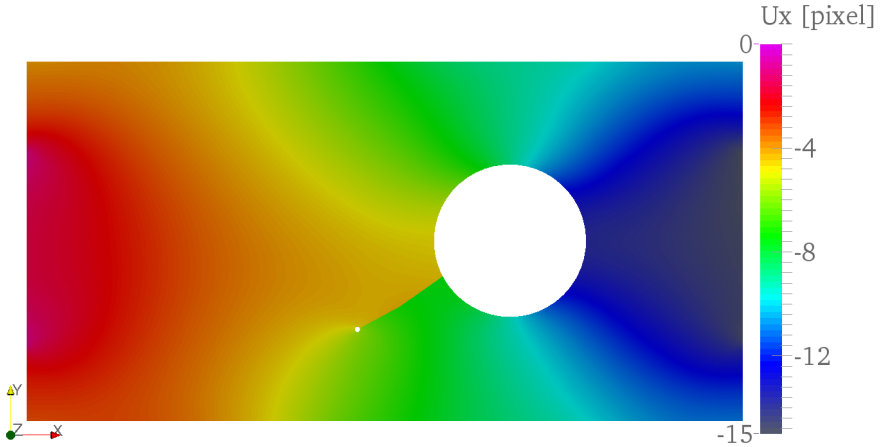

(a)

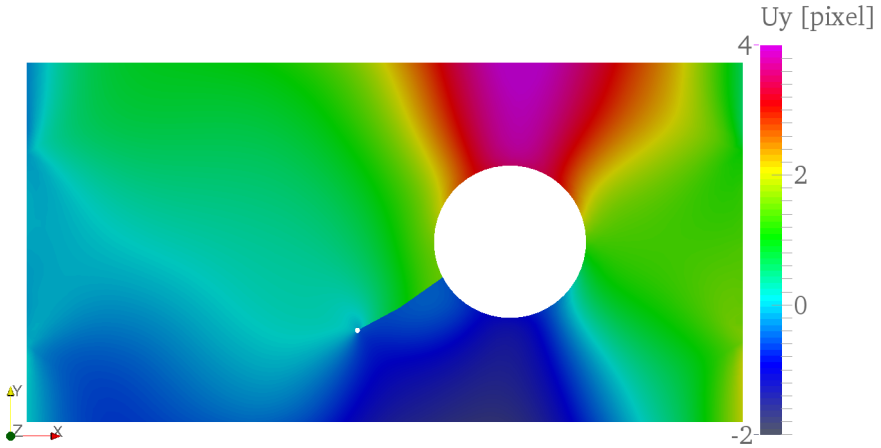

(b)

Figure 10. Horizontal and vertical displacement map (in pixel) before crack initiation.

Prepared using nmeauth.cls
DOI: 10.1002/nme

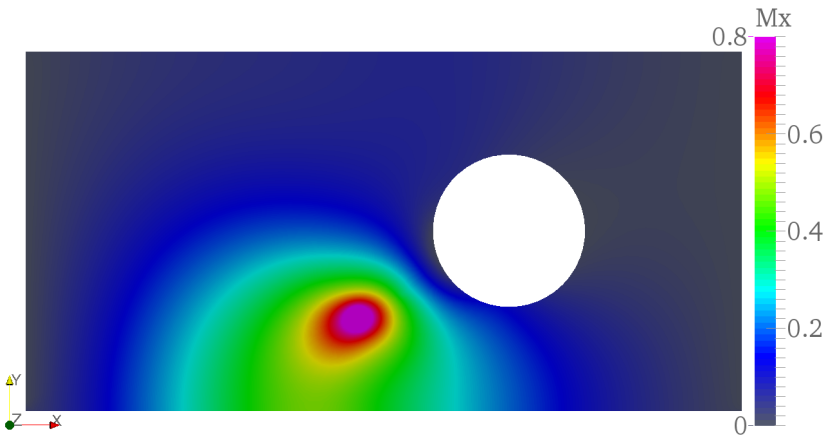

(a)

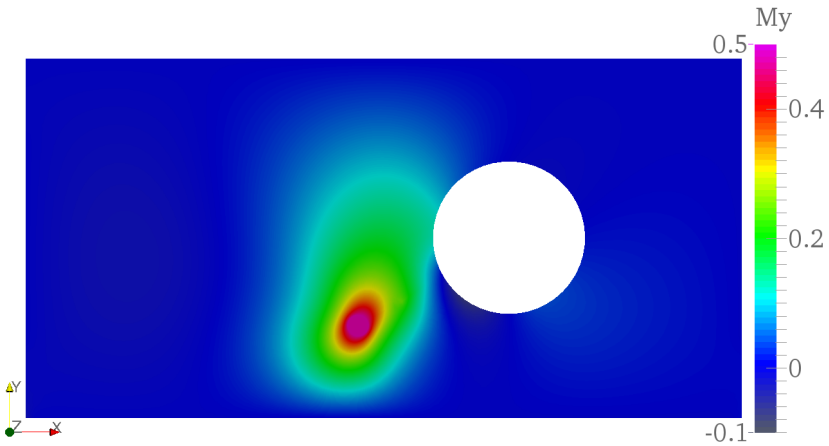

(b)

Figure 11. Example of horizontal and vertical mesh morphing map.

DOI: 10.1002/nme

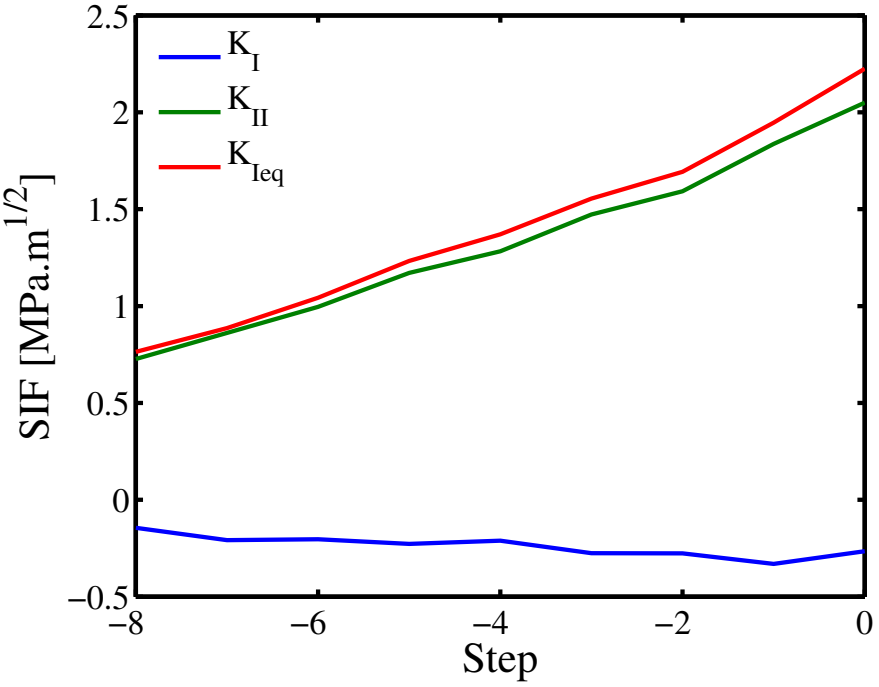

Figure 12. SIF history before crack initiation.

Prepared using nmeauth.cls
DOI: 10.1002/nme

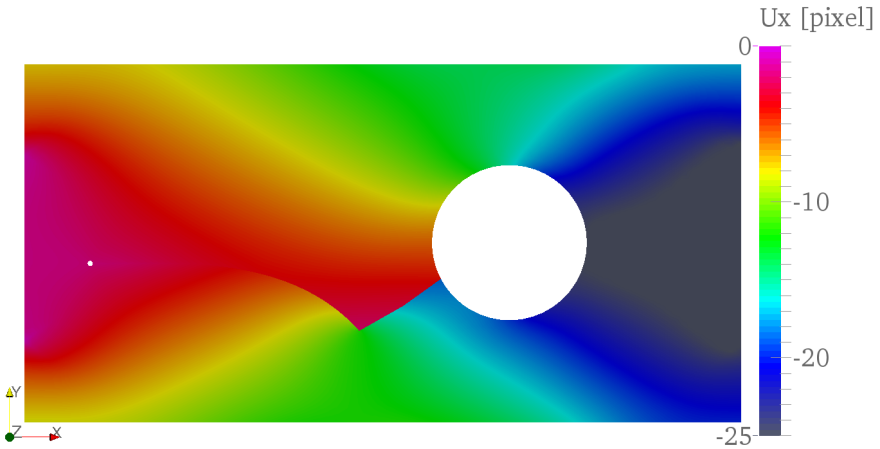

(a)

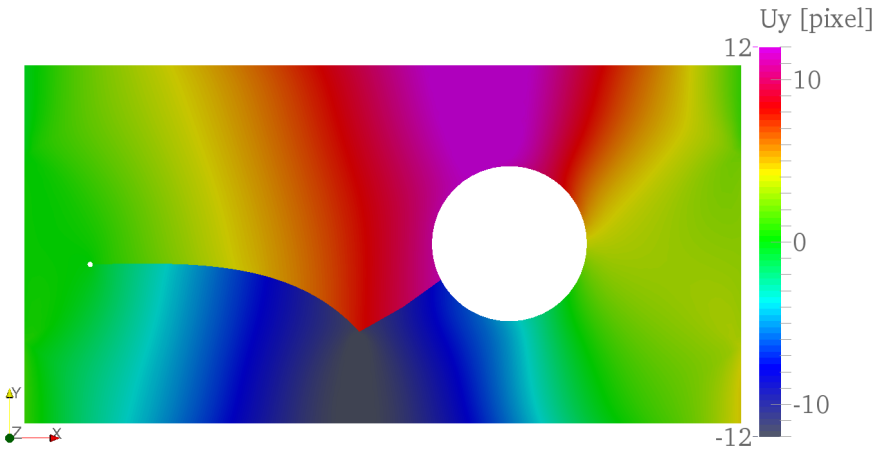

(b)

Figure 13. Horizontal and vertical displacement map (in pixel) at the end of crack propagation.

Prepared using nmeauth.cls
DOI: 10.1002/nme

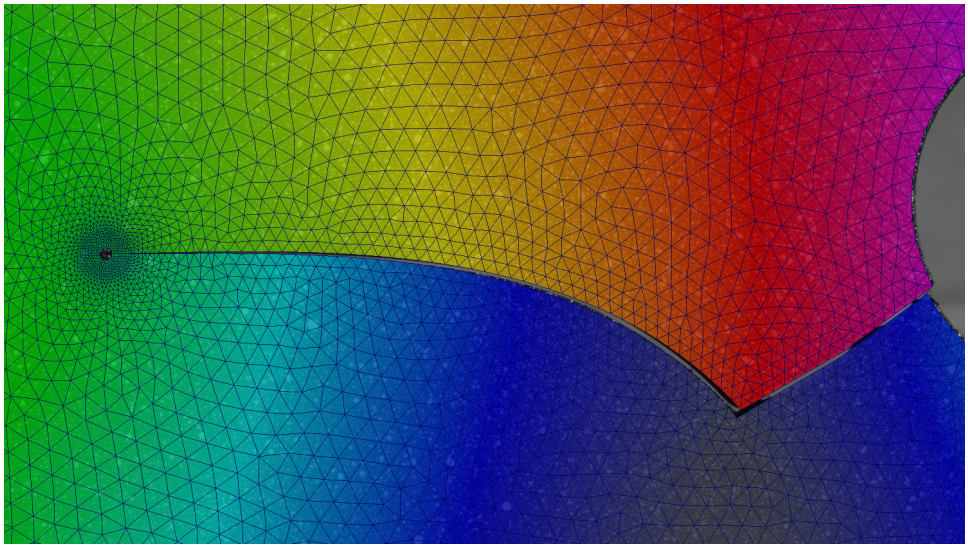

(a)

Figure 14. Zoom on the crack during propagation.

Prepared using nmeauth.cls
DOI: 10.1002/nme

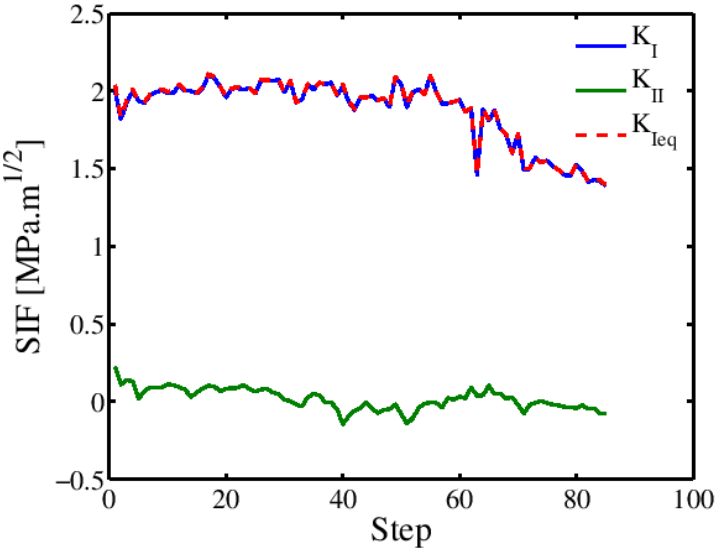

(a)

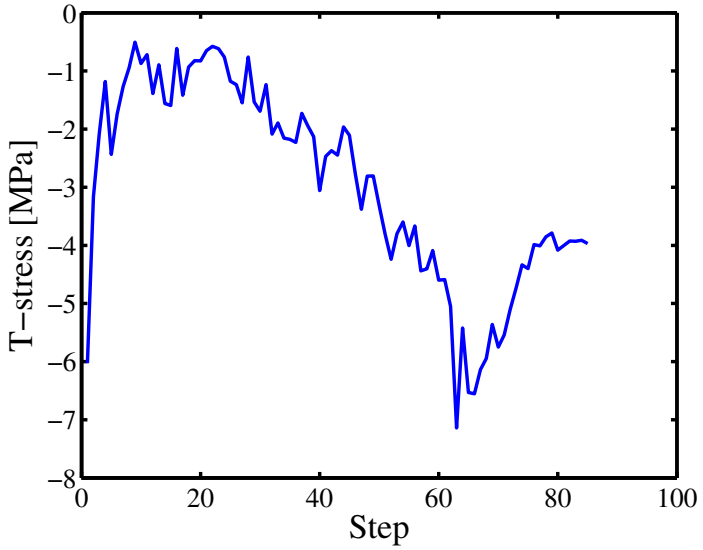

(b)

Figure 15. Evolution of SIF (a) and T-stress (b) during crack propagation.

Prepared using nmeauth.cls
DOI: 10.1002/nme

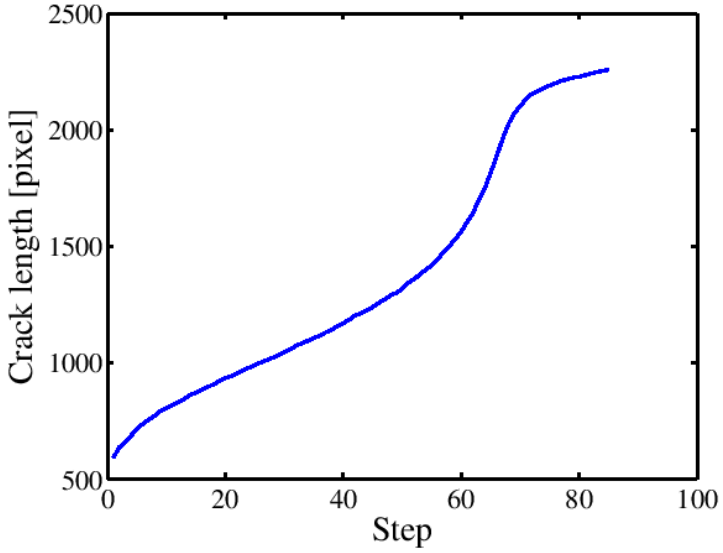

Figure 16. Evolution of crack length during crack propagation.

Prepared using nmeauth.cls
DOI: 10.1002/nme